American Mineralogist, Volume 100, pages 1411–1423, 2015

SPECIAL COLLECTION: GLASSES, MELTS, AND FLUIDS, AS TOOLS FOR UNDERSTANDING VOLCANIC PROCESSES AND HAZARDS

Aluminum and iron behavior in glasses from destabilized spinels: A record of fluid/melt-mineral interaction in mantle xenoliths from Massif Central, France†

Michel Fialin[1,*] and Christiane Wagner[2,3]

[1]Centre de Microanalyse Camparis, UPMC Univ Paris 06, IPGP, CNRS-UMR 7094, F-75005, Paris, France
[2]Sorbonne Universités, UPMC Univ Paris 06, UMR 7193, ISTeP, F-75005, Paris, France
[3]CNRS, UMR 7193, ISTeP, F-75005, Paris, France

Abstract

Infiltrations of melts (and/or fluids) in mantle rocks are witnessed by the presence of glass-bearing pockets in peridotite xenoliths brought to the surface by alkaline volcanism. Several glass-bearing pockets found around spinels corroded at different degrees were investigated for their chemical compositions, including the $Fe^{3+}/\Sigma Fe$ ratios, in two xenolith samples by electron probe microanalysis. The dissolution/recrystallization of spinels enriches the melt in alumina. We show that the spinel-derived Al^{3+} ions could have been accommodated to the melt network first as network-modifiers. Then Al^{3+} ions were network-formers using K^+ ions, extracted from the aqueous fluid upon melt dehydration, as stabilizers within the tetrahedral site. The transfer of K^+ from the aqueous fluid to the melt network is counterbalanced by an inverse transfer of CaO molecules that form crystalline phases exsolved upon eruption. The evolution of the Al content clearly shows that an increasing fraction of the spinel-derived alumina molecules was exsolved as the melt dehydration proceeded. Spinel corrosion could also be at the origin of melt oxidation through dehydrogenation reactions resulting in the formation of Al^{3+} and Fe^{3+} anionic complexes within the melt network. This study shows: (1) how the structure of the percolating melt is modified by the accommodation of chemical elements produced by the dissolution of minerals, and (2) how this process could modify the oxidation state of the melt.

Keywords: Silicate melt, mantle xenoliths, electron microprobe, $Fe^{3+}/\Sigma Fe$ measurements, melt/fluid-spinel interactions

Introduction

Glass-bearing reaction textures are worldwide known in mantle xenoliths. They usually consist of sieve-textured rims on clinopyroxene and spinel, reaction rims on orthopyroxene, and reaction pockets developed around amphibole and spinel. Besides patches of glass, the pocket assemblage contains secondary small crystals of olivine, clinopyroxene, and spinel. The textural and chemical characteristics of the reaction zones have been considered as important clues for elucidating the origin of the associated glass and intensively studied over the past two decades. However, the interpretation of the reaction textures remains controversial as it is difficult to unequivocally determine the processes and timing of their formation. Two main opposite interpretations have been argued considering the reaction textures either as products of mantle processes or resulting from reactions posterior to the xenolith entrainment in its host magma. Partial melting may have occurred in the mantle induced by heating (e.g., Maaloe and Printzlau 1979) or decompression (e.g., Su et al. 2011). It may also result from the percolation of fluids (e.g., Carpenter et al. 2002; Coltorti et al. 2000), or invading melt (e.g., Perinelli et al. 2008 and papers in Coltorti and Grégoire 2008). In contrast, these textures may have developed in crustal magma chambers or during the xenolith transport to the surface by decompression-induced partial melting, or reactions with the magma host (e.g., Carpenter et al. 2002; Shaw et al. 2006 and references therein; Wang et al. 2012). In hydrous xenoliths, the reaction textures may also have developed after the incongruent breakdown of amphibole in the mantle or during transport (e.g., Shaw and Klügel 2002; Ban et al. 2005; Ismail et al. 2008; Shaw 2009).

We present here a detailed investigation of fresh glass patches preserved in reaction textures (from few tens of μm^2- to mm^2-sized) in two lherzolite xenoliths—one anhydrous and one hydrous—from the French Massif Central. The aim of this study is to examine the exchanges, involving Al and Fe particularly, between the melt/fluid and the peridotite minerals by the means of an electron microprobe (EMP) investigation, including the measurements of the $Fe^{3+}/\Sigma Fe$ ratios.

Geological outlines

The French Massif Central is part of the Variscan belt in Western Europe. It shows an intense Cenozoic alkaline volcanism linked to the upwelling of mantle material, possibly related to a hotspot or to channeling of asthenospheric material through lithospheric fractures (e.g., Granet et al. 1995, 2000; Hoernle et al. 1995). Two distinct lithospheric domains situated north and south of the 45°30′N parallel have been recognized:

* E-mail: michel.fialin@upmc.fr

† Special collection papers can be found on GSW at http://ammin.geoscienceworld.org/site/misc/specialissuelist.xhtml.

0003-004X/15/0007–1411$05.00/DOI: http://dx.doi.org/10.2138/am-2015-5039

protogranular refractory peridotites are found in the northern domain, and fertile coarse-granular peridotites in the southern domain (as defined by Lenoir et al. 2000; see also Downes et al. 2003). Melts and fluids emanating from the mantle upwellings have greatly modified the underlying lithosphere (e.g., Downes and Dupuy 1987; Wilson and Downes 1991; Vanucci et al. 1994; Zangana et al. 1997; Xu et al. 1998; Lenoir et al. 2000; Downes et al. 2003; Féménias et al. 2004).

Our study focuses on the Devès area, which belongs to the southern lithospheric domain, near the limit between the two domains mentioned above. The Devès volcanic field is a basaltic plateau that hosted more than 150 volcanic cones aligned along a NNW-SSE trend. The volcanism is younger than 4 Ma (Maury and Varet 1980) and consists mainly of basanites (see the detailed review of the Devès volcanism by Mergoil and Boivin 1993). The Devès underlying mantle has been intensively percolated by hydrous alkaline melts leading to the crystallization of metasomatic minerals, amphibole, mica, and clinopyroxene, as well as cryptic metasomatism (Lenoir et al. 2000; Touron et al. 2008; Wagner and Deloule 2007).

Petrography of the xenoliths

The xenoliths come from the consolidated scoriae cone of Mont Gros (quoted as MG below) near Alleyras (N44°54′, E3°41′). The xenolith-entraining magma is a Si-undersaturated alkaline basanite (Jardin 1973). We have collected 150 ultramafic xenoliths and discarded any xenoliths with dusty olivine and pyroxene or showing oxidation due to heating by the host magma. The dominant petrologic type is a spinel lherzolite that contains amphibole in 20% of the xenoliths. Amphibole is a pargasite that forms either disseminated crystals interstitial to olivine, clinopyroxene, orthopyroxene, and spinel, or developed around spinels, whereas an amphibole selvage that partially surrounded the peridotite is sometimes observed. Half of the spinel lherzolite xenoliths show glassy percolation paths of an invading melt/fluid and glass-bearing reaction pockets. The reaction pockets are either interstitial or developed around spinel ± amphibole. It should be noticed that in half of the amphibole-bearing xenoliths, amphibole is not surrounded by a reaction pocket. For this study we focus on two spinel lherzolite xenoliths: anhydrous sample MG102 and sample MG54 with relicts of amphibole. Both samples are planar-faced fresh xenoliths of ~10 cm in diameter with remnants of a vesicular basanite crust (Figs. 1 and 2). They show glass-bearing reaction zones often located around spinel or disseminated in the lherzolite. A detailed petrographic description of the two samples is given in Appendix A.

In the following, "secondary" refers to the neoformed phases observed in the reaction pockets, and "primary" to the original phases of the lherzolite. In sample MG102 reaction features are observed at the contact with the host basanite (Fig. 1): orthopyroxene shows dissolution along former cleavages (Fig. 1d) and clinopyroxene has a sieve texture, which may invade the whole grain (Fig. 1b). Close to the contact with the host basanite spinel develops a thick (up to 700 μm) zone of opaque spinel surrounding the brown core (Fig. 1e, zone 1) and is embedded in a large vesicular glass-bearing reaction zones including secondary olivine and clinopyroxene. Glass-bearing reactional paths penetrate the xenolith from the contact with the basanite (Fig. 1b). However, no such intense interaction can be evidenced further inside the xenolith (zones 3 and 4) as clinopyroxene is not sieve-textured and spinel poorly corroded (Fig. 1f) or uncorroded (Fig. 1g). Sample MG54 shows no evidence of reaction with the host basanite and no glass-bearing reactional paths throughout the xenolith (Fig. 2). The glass-bearing reaction zones only occur around spinel (Fig. 2) and show relicts of amphibole in some locations (Fig. 2d).

Detailed description of reaction zones around corroded spinels

Figures 3 to 6 show typical reaction zones in the MG54 and MG102 samples, featured by the backscattered (BSE) images as well as the elemental maps of Al, alkalis, Ca, and Mg expressed as oxide-wt%. The reaction zones developed around primary spinel in contact with primary orthopyroxene. Primary spinel exhibits a sieve-textured rim consisting of small secondary spinel grains in a glass framework that embeds secondary olivine and clinopyroxene. We note first in the BSE images the presence of abundant bubble-like voids (black) corresponding to formerly volatile-filled vesicles that formed at low pressure or upon eruption. The presence of former H_2O-rich (instead of CO_2-rich) fluid is likely as amphibole is present in numerous Mont Gros lherzolite samples (see above).

In sample MG54, spinel appears as white shades in the BSE image (Figs. 3a and 3b) and orange in the Al_2O_3 map (Fig. 3c). The residual melt forms a connected framework, blue-green in the Al_2O_3 map (Fig. 3c) and white in the Na_2O+K_2O map (Fig. 3e). In sample MG102 the primary spinels from zone 4 exhibit a very limited sieve-textured rim around a corroded core (Fig. 4) and are surrounded by poorly developed reaction zones (Fig. 4a) similar to those of sample MG54. However, in contrast to sample MG54, the major feature of sample MG102 is the large degree of corrosion of the primary spinel evidenced in some locations, e.g., zone 1 (Figs. 1c, 1e, 5a, 5b, and 5c). The core of the relict primary spinel exhibits large corrosion-induced embayments and perforations (red arrows in Fig. 5b). The highly corroded rim shows development of a large amoeboid-shaped spongy corona consisting of numerous small secondary Al-rich spinel grains (white-green-red in Fig. 5c) embedded in a dense glass framework (green in Fig. 5c; white in Fig. 5e). Moreover, in some locations of the MG102 sample, primary spinels are no longer observed and only few blebs of secondary spinel still remain visible (Fig. 1c, zone 2; Fig. 6).

Analytical procedure

The chemical composition of minerals and glasses, as well as the glass $Fe^{3+}/\Sigma Fe$ ratios, were determined with a Cameca SXFive electron microprobe equipped with five wavelength-dispersive spectrometers (WDS). Three of the WDS were equipped with TAP monochromators (two regular –660 mm^2 TAP and one large-area –1320 mm^2 TAP) to collect the Fe$L\alpha$ peak data that are used by the procedure for the determination of the $Fe^{3+}/\Sigma Fe$ ratios as explained hereafter. WDS analyzes were performed using the following standards: diopside for Si, Mg, and Ca; orthose for Al and K; albite for Na; apatite Durango for P; $MnTiO_3$ for Mn and Ti; hematite for Fe; scapolite for Cl; topaz for F.

The determination of the $Fe^{3+}/\Sigma Fe$ ratios, known as the "peak shift" method is detailed in Fialin et al. (2001, 2004, 2011) and can be summarized as follows. First, each glass analysis presented in Table 1 represents the average of 10 neighboring locations probed with a 15 kV, 10 nA, and 20 μm beam at a single glass pocket.

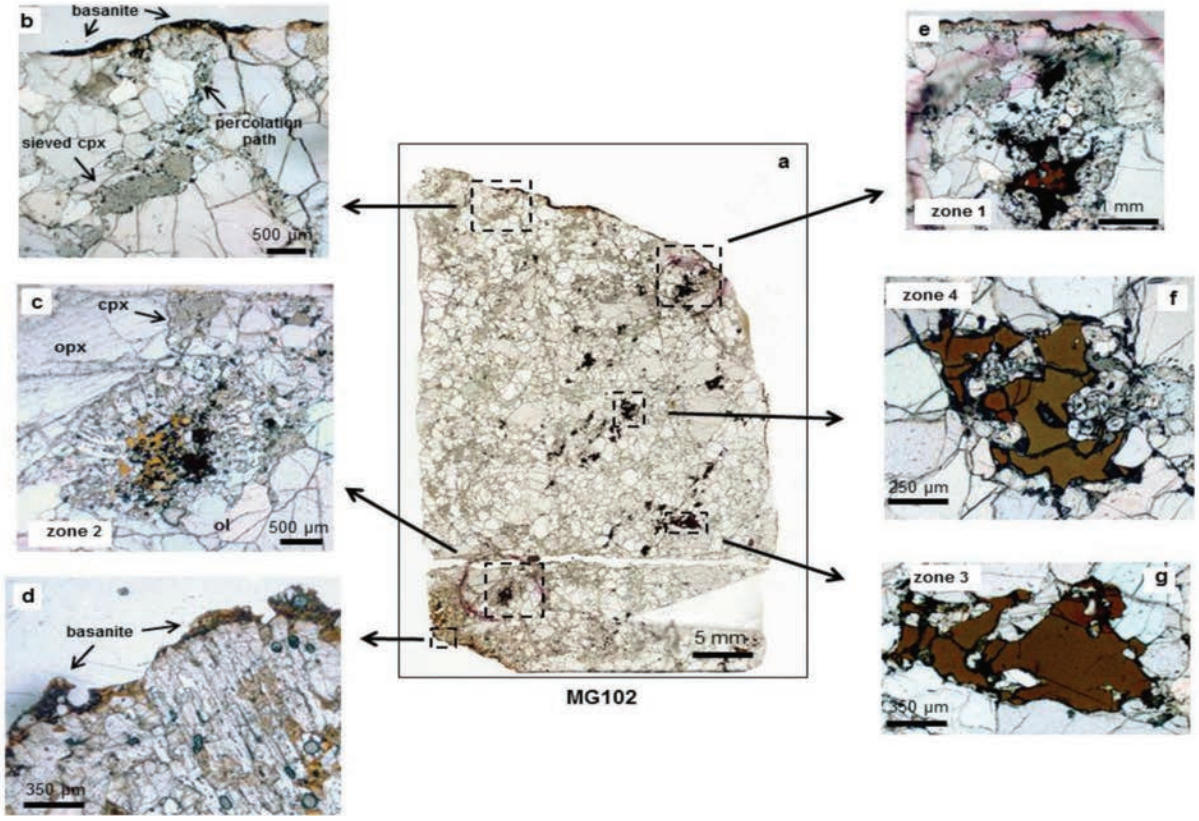

Figure 1. Sample MG102. General view (**a**) and detailed boxes (**b** to **g**). (**b**) Lherzolite—host basanite contact showing sieve-textured clinopyroxene (cpx) and glassy percolation paths. (**c**) Reaction zone developed around spinel in zone 2. Cpx, orthopyroxene (opx), and olivine (ol) refer to primary minerals. Note that cpx is sieve-textured. Details of the reaction zone are given in Figure 6. (**d**) Destabilized opx at the contact with the host vesicular basanite. (**e**) Reaction zone developed around spinel in zone 1. (**f**) Poorly corroded spinel 4.7 in reaction zone 4 (details in Fig. 4). (**g**) Uncorroded spinel from zone 3. All views in transmitted light. (Color online.)

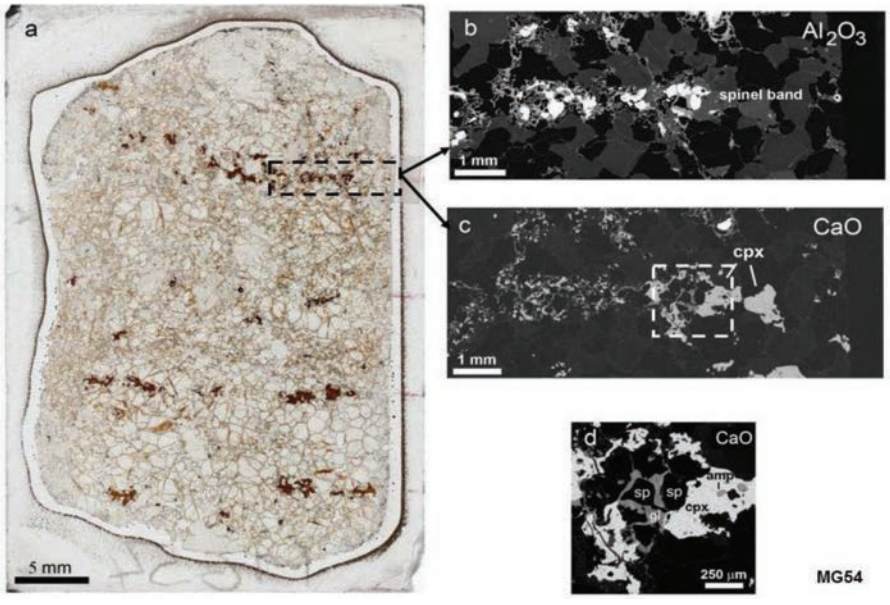

Figure 2. Sample MG54. (**a**) General view (in transmitted light) and detailed boxes (**b** to **d**). (**b** and **c**) Al_2O_3 (**b**) and CaO (**c**) elemental maps showing the glassy framework of the reaction zones developed in spinel band. (**d**) Detail (box in **c**) of the reaction zone developed around spinel (sp, in black) showing glass (gl) and relict amphibole (amp) in cpx. (Color online.)

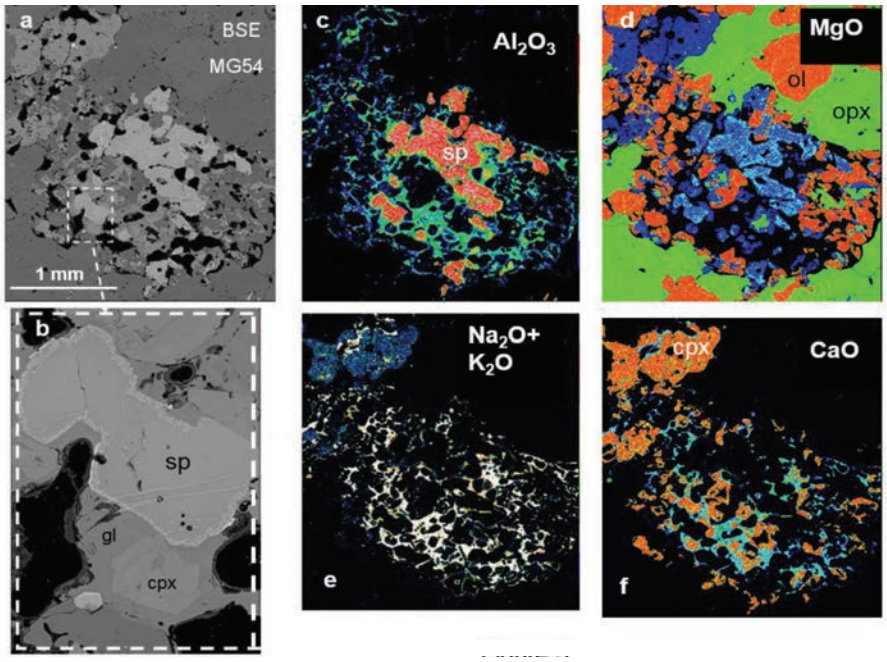

FIGURE 3. Reaction zone developed around spinel in sample MG54. (**a**) General view (BSE image). (**b**) Detail boxed in **a**. (**c**–**f**) Elemental maps. (**c**) Al_2O_3; orange = sp, blue-green = glass. (**d**) MgO; orange = ol, green = opx, light blue = sp, blue = cpx. (**e**) Na_2O+K_2O; white = gl, blue = cpx. (**f**) CaO; orange = cpx; dark blue = gl. Abbreviations as in Figures 1 and 2. (Color online.)

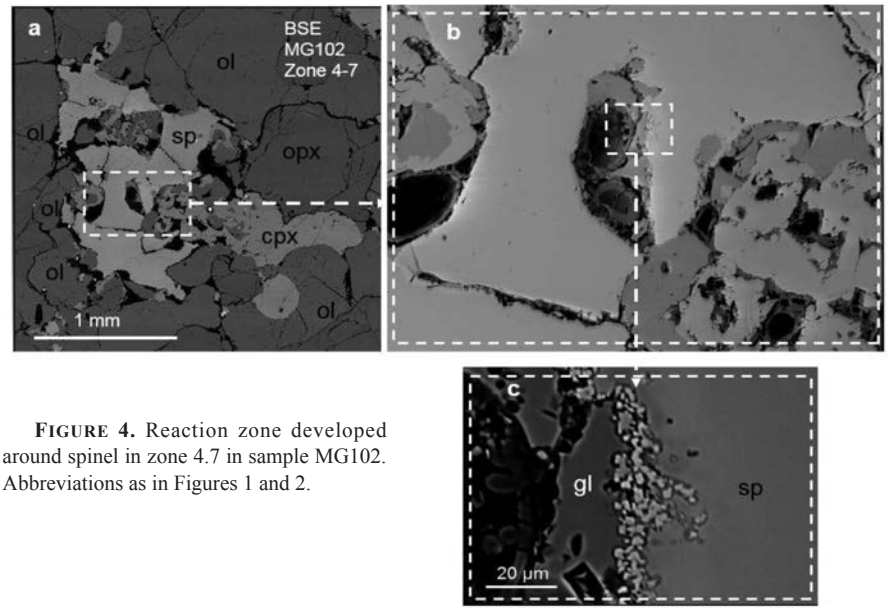

FIGURE 4. Reaction zone developed around spinel in zone 4.7 in sample MG102. Abbreviations as in Figures 1 and 2.

The dwell time for each element was 10 s on peaks plus 10 s on backgrounds. Second, the wavelength positions of the Fe$L\alpha$ peak, necessary for $Fe^{3+}/\Sigma Fe$ ratios determination, were measured on each of the 10 locations with the same spot beam conditions except for the intensity that was increased to 80 nA. We thus obtained a single $Fe^{3+}/\Sigma Fe$ value per glass pocket investigated. We carefully checked for the common pitfalls encountered with the use of the peak shift method applied to glasses, particularly, i.e., the roles played in the position shift of the Fe$L\alpha$ peak by: (1) beam-induced oxidation, and (2) matrix effects. (1) Beam-induced oxidation causes the shift of the Fe$L\alpha$ peak toward lower wavelength with subsequent increase of $Fe^{3+}/\Sigma Fe$. To overcome this difficulty, eight replicate measurements of the peak position were performed at each of the 10 glass locations. The "true" peak position was evaluated as the zero time intercept of the branch of parabola fitting the eight values [refer to Figs. 6 and 7 in Fialin et al. (2001) and Fig. 5 in Fialin et al. (2004), for examples]. (2) The composition of the studied glasses is similar to those of the standards used to construct the calibration curves, which allows avoiding any Fe$L\alpha$ peak shift due to matrix effects [refer to the extended discussion in Fialin et al. (2001) paragraph "Limitation" p. 462]. High-spatial resolution BSE images were obtained with an analytical Carl Zeiss Supra 55VP field-emission scanning electron microscope (FE-SEM) equipped with a Bruker energy-dispersive spectrometer (EDS).

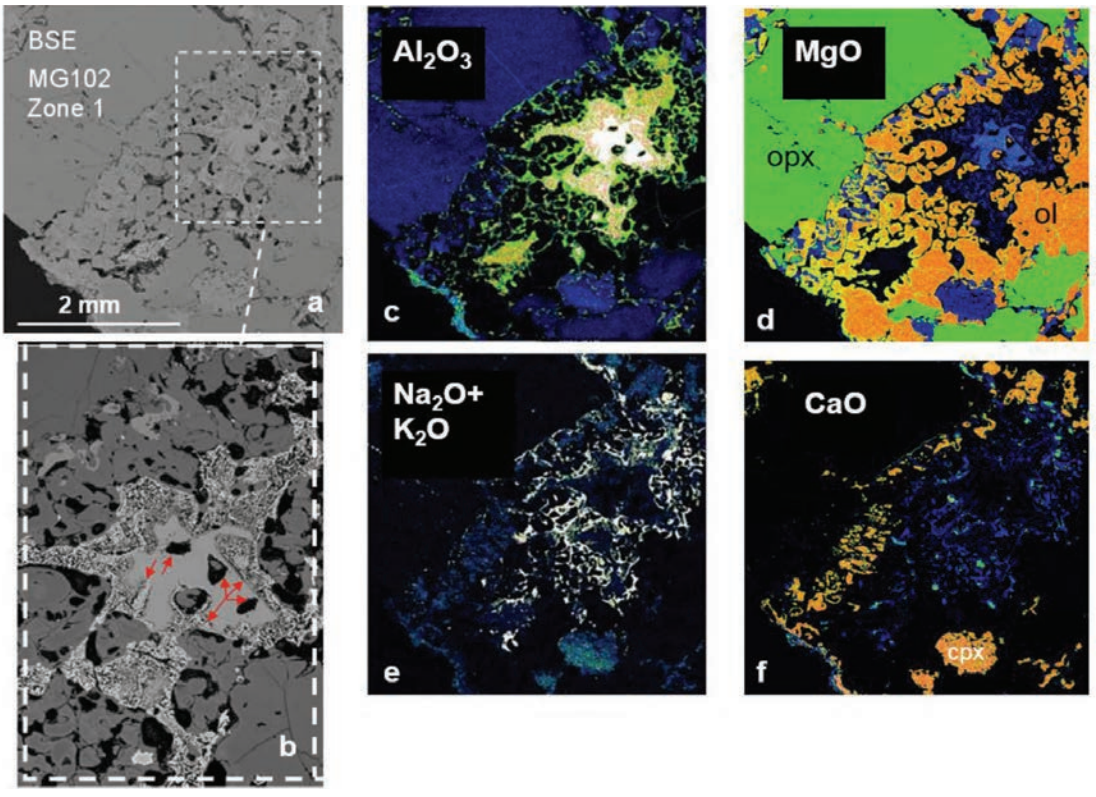

Figure 5. Reaction zone developed around spinel in zone 1 of sample MG102. (**a**) General view **(**BSE image). (**b**) Detail boxed in **a**. The red arrows indicate corrosion features of the primary sp core. (**c**–**f**) Elemental maps. (**c**) Al_2O_3; white = primary sp, green = gl, mixed white-green-red = corona of secondary sp around the central primary sp. (**d**) MgO; orange = ol, green = opx, light blue = sp, dark blue = cpx. (**e**) Na_2O+K_2O; white = gl, blue = cpx. (**f**) CaO; orange = cpx, dark blue = gl. Abbreviations as in Figures 1 and 2. (Color online.)

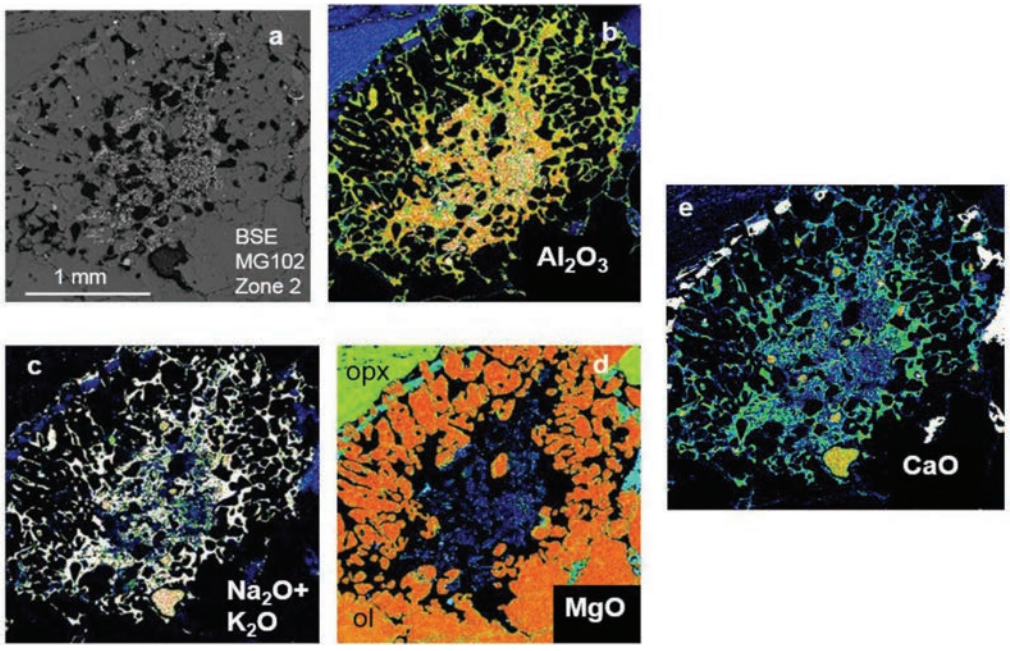

Figure 6. Reaction zone developed around spinel in zone 2 of sample MG102. (**a**) General view (BSE image). (**b**–**e**) Elemental maps. (**b**) Al_2O_3; white-green-red = gl network. (**c**) Na_2O+K_2O; white = gl, blue = cpx. (**d**) MgO; orange = ol, green = opx, blue = sp, turquoise = cpx. (**e**) CaO; white = cpx, green = gl. Abbreviations as in Figures 1 and 2. (Color online.)

TABLE 1. Glass compositions

(wt%)	MG54 (A1)	MG54 (C1-1)	MG54 (C1-2)	MG54 (C2-1)	MG54 (C2-2)	MG54 (D1-2)	MG54 (D1-7)	MG54 (D1-8)	MG54 (D2-1)	MG54 (D2-2)	e.s.d. (2σ)	MG102 (zone 1)	MG102 (zone 2)	MG102 (zone 3)	MG102 z 4-2, 4-3,4-4	MG102 (zone 4-7)	e.s.d. (2σ)	dla (ppm)
SiO_2	56.91	54.94	55.36	55.38	54.75	54.74	55.00	54.97	55.60	55.16	0.83	59.45	61.41	58.16	57.66	55.10	0.84	185
TiO_2	0.83	1.28	1.23	1.35	1.29	1.73	1.65	1.67	1.90	2.04	0.31	0.32	0.48	0.32	0.35	0.40	0.29	193
Al_2O_3	19.12	18.78	18.64	19.19	19.13	19.20	18.96	19.11	19.50	19.55	0.36	19.58	18.51	20.67	20.59	21.18	0.36	156
Cr_2O_3	0.07	0.22	0.11	0.04	0.02	0.06	0.04	0.07	0.17	0.22	0.1	0.06	0.12	0.20	0.13	0.15	0.10	256
FeOT	3.15	3.78	3.73	3.49	3.40	3.52	3.43	3.44	3.46	3.73	0.3	2.59	2.71	3.18	3.30	3.75	0.28	492
MnO	0.06	0.08	0.11	0.09	0.07	0.09	0.09	0.10	0.08	0.09	0.05	0.01	0.12	0.06	0.06	0.06	0.05	376
MgO	3.90	4.67	4.66	4.15	3.92	4.21	4.41	4.31	4.10	4.34	0.47	2.30	2.09	3.57	3.68	4.01	0.39	93
CaO	8.02	8.69	8.13	8.40	8.49	8.55	8.28	8.28	8.79	8.96	0.83	2.83	2.53	6.48	6.95	8.31	0.73	271
Na_2O	4.51	3.56	4.16	4.32	4.98	4.53	4.90	4.90	3.22	3.08	0.92	7.55	7.02	6.37	5.96	5.41	1.01	480
K_2O	2.31	1.81	1.87	1.94	1.95	1.79	1.84	1.84	1.72	1.74	0.21	4.66	5.07	0.97	0.83	0.52	0.47	186
P_2O_5	0.29	1.40	1.46	0.73	0.71	0.45	0.44	0.45	0.27	0.31	0.34	0.06	0.07	0.07	0.09	0.10	0.11	116
Cl	0.07	0.11	0.10	0.09	0.09	0.07	0.07	0.07	0.07	0.08	0.02	0.09	0.07	0.18	0.21	0.24	0.02	145
F	0.13	0.15	0.13	0.08	0.06	0.09	0.09	0.11	0.16	0.14	0.07	0.05	0.07	0.03	0.03	0.02	0.06	575
Total	99.38	99.47	99.71	99.25	98.87	99.03	99.20	99.32	99.03	99.42		99.59	100.27	100.26	99.83	99.25		
$Fe^{3+}/\Sigma Fe$	0.65	0.75	0.69	0.68	0.66	0.63	0.68	0.72	0.62	0.65		0.57	0.63	0.74	0.88	0.99		
FeO	1.10	0.95	1.16	1.12	1.15	1.30	1.10	1.00	1.31	1.31		1.12	1.00	0.83	0.40	0.04		
Fe_2O_3	2.28	3.15	2.86	2.64	2.49	2.47	2.60	2.72	2.38	2.70		1.64	1.90	2.62	3.23	4.13		
Norm CIPW																		
Qz	2.4	6.4	4.6	2.8		0.8			7.6	7.2					1.2			
Or	13.7	10.7	11.1	11.5	11.3	10.6	10.9	10.9	10.2	10.3		27.6	30.0	5.7	4.9	3.1		
Lc																		
Ab	38.1	30.1	35.1	36.5	42.1	38.3	41.4	41.4	27.2	26.0		44.1	49.1	53.8	50.4	45.7		
Ne												10.7	5.5					
An	25.1	29.9	26.6	27.2	24.2	26.7	24.3	24.7	33.6	34.3		5.7	4.0	24.9	26.9	31.7		
Cor																		
Aeg																		
Di	10.0	3.0	3.3	7.6	10.4	9.5	10.0	9.3	5.4	5.0		6.2	6.3	5.3	5.4	6.0		
Wo		0.2				0.3	0.5	0.6	0.5	0.7						0.4		
Hy	5.1	10.3	10.1	6.9	2.7	6.1	3.6	3.5	7.7	8.5				6.1	6.7	6.6		
Ol					1.6		2.0	2.1				2.2	1.6	0.3		0.4		
Mt	1.3		0.5		0.2							2.4	2.2	1.9	0.5			
Ht	1.4	3.2	2.5	2.6	2.4	2.5	2.6	2.7	2.4	2.7			0.4	1.3	2.9	4.1		
Ilm	1.6	2.2	2.3	2.6	2.5	2.9	2.5	2.3	2.9	3.0		0.6	0.9	0.6	0.7	0.2		
Ap	0.7	3.2	3.4	1.7	1.6	1.0	1.0	1.0	0.6	0.7		0.1	0.2	0.2	0.2	0.2		
Sp		0.3				0.5	0.8	1.1	0.9	1.2						0.7		
Pv																		
Total	99.4	99.5	99.5	99.4	99.0	99.2	99.6	99.6	99.0	99.6		99.6	100.2	100.1	99.8	99.1		

Note: [a] For each elements, the detection level (dl) represents an average value calculated from the 15 analyses listed; e.s.d. = Estimated standard deviation at 2σ.

CHEMICAL RESULTS

We focus below on the composition of spinel and glass from the reaction pockets, whereas a summary of the chemical composition of the primary and secondary silicate minerals is given in Appendix B.

Spinel

The compositions of the spinels in both MG54 and MG102 samples are given in Table 2. Marked compositional differences between uncorroded primary spinel cores and secondary spinel are observed: for example in sample MG54, secondary spinel is Cr_2O_3 enriched (17.3–25.3 wt%) and Al_2O_3 depleted (43.6–51.0 wt%) compared to primary spinels (13.9–16.5 wt% Cr_2O_3 and 50.3–53.0 wt% Al_2O_3). These differences are dramatically increased for the highly corroded spinels in zones 1 and 2 of the MG102 sample, which have a variable and extremely high cr* (21.3—up to 63.4 in zone 2).

Glass

The glasses are alkali-rich and Si-saturated or oversaturated, except the glasses from the two most destabilized zones 1 and 2 of MG102, which are Si-undersaturated (11 and 5% normative nepheline, respectively; Table 1). The TAS (total alkali-silica) diagram (Fig. 7) shows that glasses from MG54 have a restricted range of composition compared to those of sample MG102, in which glasses from zones 1 and 2 reach a trachytic composition. Such glasses are worldwide known in mantle xenoliths (Coltorti and Grégoire 2008). In sample MG102 the glass from the two reaction pockets with highly corroded spinels from zones 1 and 2 shows high silica and alkali compared to the glass in the pockets from the zones 3 and 4, in which spinel is poorly corroded (Table 1; Fig. 7). The glasses from zones 3 and 4 have a composition similar to that of the glasses from MG54, but Al- and Fe^{3+}-richer and K-depleted (Fig. 8). Glasses from sample MG54 and zones 3 and 4 of sample MG102 contain between 3.6–4.7 wt% MgO, while glasses associated with highly corroded spinels (MG102, zones 1 and 2) are less magnesian (~2 wt% MgO).

DISCUSSION

Origin of the glassy pockets

Before discussing the behavior of aluminum and iron in glass from the reaction pockets around spinel, we first examine the glass origin. The xenoliths display distinct reaction features suggesting different genetic processes that are discussed below based on the previously exposed textural and chemical characteristics of the reaction zones and compared to experimental results.

Xenolith-host magma interaction after entrainment. Some features are clearly related to interaction between the xenolith and

TABLE 2. Spinel compositions (average of 10 spot analyses)

	MG54				MG102						
	primary		secondary		primary		secondary				dl[a]
		range		range	zones 1–4	range	zones 3,4	range	zones 1,2	range	(ppm)
SiO_2	0.07	<0.08	0.12	<0.13	0.02	<0.08	0.32	<0.35	0.09	<0.23	203
TiO_2	0.07	0.01–0.10	0.62	0.35–0.83	0.01	<0.02	0.09	0.05–0.16	0.31	0.11–0.52	221
Al_2O_3	52.05	50.30–53.01	43.84	43.64–51.01	55.37	54.35–56.91	50.71	49.53–51.95	27.58	19.79–47.89	175
Cr_2O_3	15.55	13.93–16.46	24.47	17.29–25.25	11.61	11.36–12.30	16.53	14.83–18.02	38.77	26.87–50.05	285
FeO	11.88	10.82–13.69	9.32	6.73–11.79	12.55	11.37–13.12	11.31	10.49–11.72	13.92	10.54–18.80	507
MnO	0.12	0.06–0.16	0.12	0.06–0.15	0.08	0.03–0.15	19.61	0.12–0.19	0.10	0.08–0.19	395
MgO	20.17	18.72–20.53	20.81	19.00–23.15	19.20	18.10–19.78	0.16	18.79–19.83	16.49	13.02–20.13	118
NiO	na	–	na	–	0.44	0.39–0.64	0.24	0.21–0.35	0.19	0.04–0.41	400
Total	99.91		99.31		99.27		98.98		97.45		
Si	0.002		0.003		0.000		0.008		0.003		
Ti	0.001		0.013		0.000		0.002		0.007		
Al	1.616		1.402		1.716		1.594		0.976		
Cr	0.324		0.525		0.241		0.349		0.920		
Fe	0.262		0.211		0.276		0.252		0.350		
Mn	0.003		0.003		0.002		0.786		0.002		
Mg	0.792		0.842		0.752		0.004		0.738		
Ni					0.012		0.005		0.006		
Fe^{3+}	0.05		0.04		0.04		0.04		0.08		
Fe^{2+}	0.21		0.17		0.23		0.22		0.27		
cr*	16.2	14.9–17.5	26.7	18.2–27.2	12.1	11.7–12.9	17.6	15.8–19.3	46.5	21.3–63.9	
$Fe^{3+}/\Sigma Fe$	0.20		0.20		0.15		0.14		0.24		

Notes: Mineral formulae were calculated using normalization on three cations. n.a.= not analyzed; cr* = 100×molar Cr/(Cr+Al+Fe^{3+}).
[a] For each elements, the detection level (dl) represents an average value calculated from the five analyses.

the host magma. In sample MG102, the most corroded spinels are observed in the reaction zones 1 and 2 close to the contact with the basanite host (Fig. 1). The composition of the associated glass (ne-normative) is quite distinct from that of glasses (Si-saturated or oversaturated) from reaction zones further inside the xenolith (Table 1), where no host melt percolation was observed. Its composition matches that of experimental melts obtained by incongruent dissolution of orthopyroxene in Si-undersaturated alkaline melt at one atmosphere (Shaw et al. 1998; Shaw and Dingwell 2008). In these experiments, the dissolution of orthopyroxene is followed by the crystallization of new olivine + clinopyroxene from the boundary layer melt. According to these authors, clinopyroxene likely results from a local clinopyroxene saturation after the diffusion of calcium toward the orthopyroxene. In sample MG102 secondary clinopyroxene crystals are indeed concentrated close to the primary orthopyroxene (Figs. 5 and 6). Moreover, the reaction zones contain a high amount of olivine (Figs. 3–6), a fact mentioned in experimental studies (Shaw et al. 1998; Shaw 1999) in relation to the alkali-rich character of the reacting infiltrating melt, which stabilized olivine (Kushiro 1975). The melt produced by the incongruent dissolution of orthopyroxene causes then the destabilization of spinel (e.g., as proposed by Shaw and Dingwell 2008), and the crystallization of Cr-richer secondary spinel in the destabilized rim (Table 2). The influence of the host magma seems to be limited to the vicinity of the contact with the xenolith, as the interior of the xenolith shows no traces of percolation of the host magma and no sieve-textured clinopyroxene (Fig. 1), while the reaction zones around spinel (e.g., zone 4 in sample MG102, Fig. 1f) are less developed with a glass of quite different composition (Table 1). Other mechanisms are thus required in both samples for the formation of reaction zones away from host melt influence.

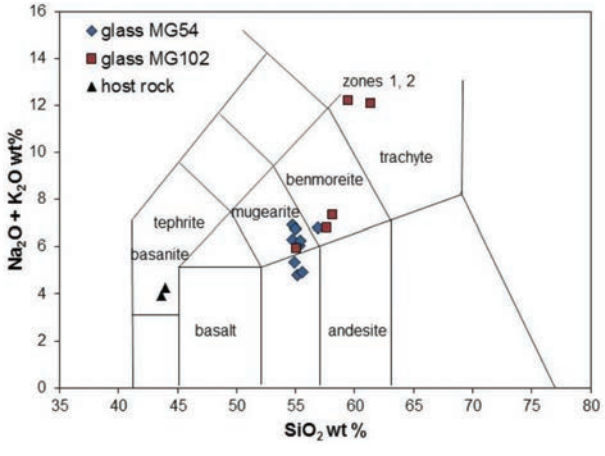

FIGURE 7. Range of glass compositions from samples MG54 (blue diamond) and MG102 (red square) compared to host magmatic rocks of Mont Gros (black triangles; data from Jardin 1973) plotted in the total alkali vs. silica diagram after Le Bas et al. (1986). (Color online.)

In situ and decompression melting. Silicic and alkaline liquids may be obtained by low-degree disequilibrium melting in the mantle at *P* about 1–1.5 GPa (Draper and Green 1999; Lo Cascio et al. 2008). These experimental liquids are anhydrous, sodic, potassic (Draper and Green 1999) or not potassic (Lo Cascio et al. 2008), and Si-undersaturated. In contrast MG102 glasses from the reaction zones 3 and 4 (located in the interior of the xenolith) are Si-saturated or Si-oversaturated, and, thus, not consistent with small degrees of in situ partial melting of the lherzolite. On the other hand, although lherzolite xenoliths are abundant in the Mont Gros occurrence, only about half of them show glass-bearing reaction pockets or glass veins. This suggests that decompression melting is not the main—or single—mechanism responsible for the formation of the reaction zones.

Breakdown of amphibole. About half of the amphibole-bearing xenoliths from Mont Gros show reaction zones around amphibole. The formation of glass by decompression-induced breakdown of amphibole has been proposed by several authors (e.g., Frey and Green 1974; Francis 1976; Stosch and Seck 1980;

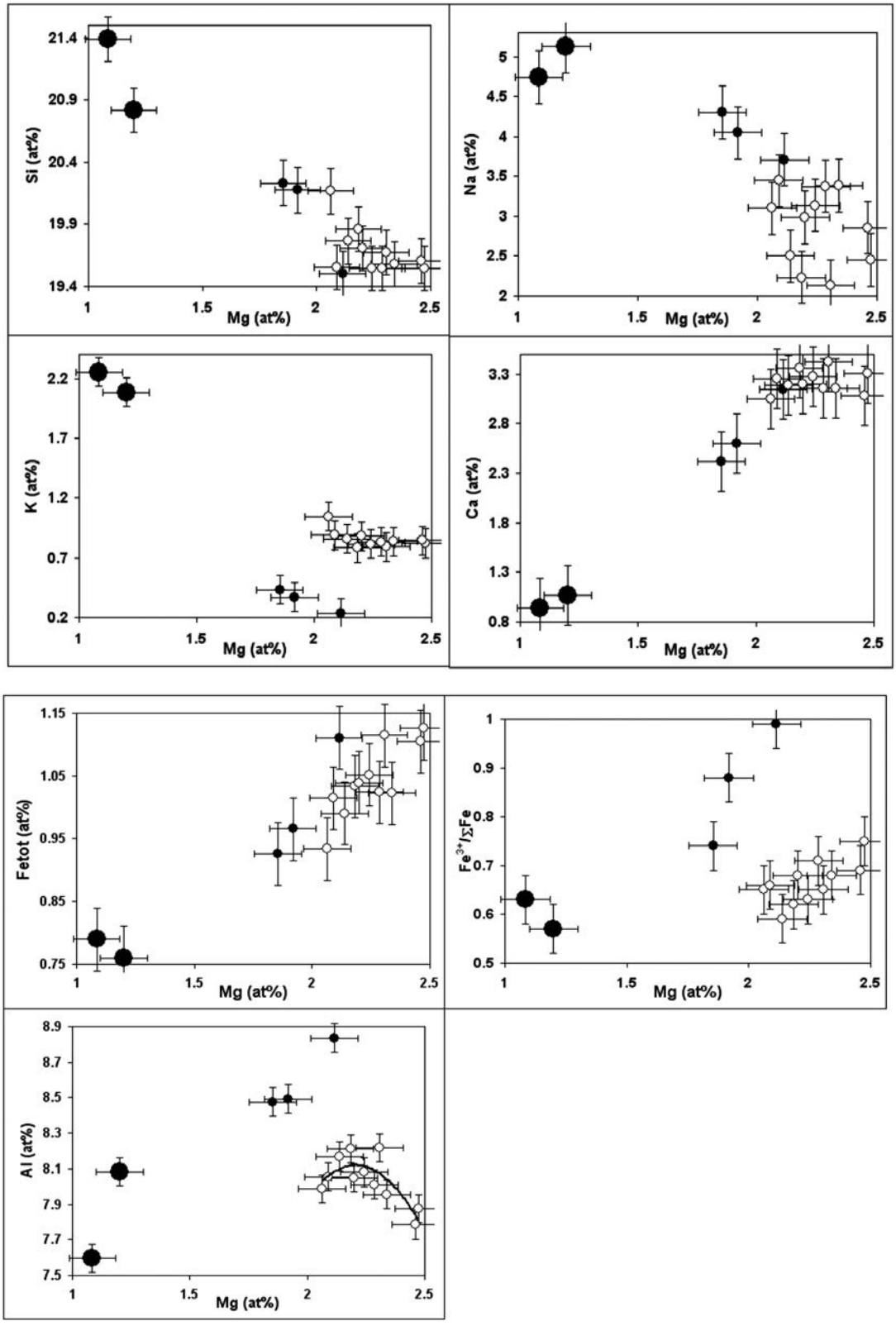

FIGURE 8. Variations of glass compositions vs. Mg expressed in atom percent (at%) for samples MG54 (open circles) and MG102 (filled circles). Large filled circles correspond to glass compositions from MG102 reaction zones 1 and 2, which exhibit highly corroded spinels. The Al vs. Mg trend for MG54 is reinforced by the least-squares fitted second-order polynomial (solid line).

Chazot et al. 1996; Yaxley et al. 1997; Ismail et al. 2008). In sample MG54, small amphibole crystals in the reaction zones are likely relicts of former destabilized amphibole (Fig. 2d).The glass FeO_{Total}/MgO ratio (0.8 compared to 0.3 for the amphibole) is consistent with the ensuing fractional crystallization of Mg-richer secondary olivine, clinopyroxene, and spinel in the reaction zones. The glass is enriched in alkalis compared to the amphibole with variable but high-Na_2O contents (up to 5.0 wt%), a content higher than that expected from the crystallization of secondary clinopyroxene after the amphibole breakdown. This suggests the addition of a Na-rich melt (or fluid?) of untraceable origin, which may have induced—or contributed to—the melting of pre-existing amphibole. The melting of amphibole may have occurred either in the mantle before or during the entrainment of the xenolith in the host magma, but at present we cannot argue further on this point. The resulting melt reacts then with the primary minerals in a manner similar to that described above for the role of the host magma. Last, although amphibole has not been found in sample MG102, amphibole may have completely melted and its involvement in the formation of the glass cannot be discarded. Moreover, even if amphibole is involved, the glass high-Na_2O content (5.4–6.4 wt%) requires the contribution of a Na-rich agent, as proposed above for sample MG54. The infiltration is likely to have occurred shortly before eruption, as a melt fraction was preserved in the reaction pockets and as there is no diffusion (at the micrometer scale) in the primary minerals adjacent to the pockets.

Dissolution-crystallization mechanism of spinels: The fate of the spinel-derived alumina

As discussed above, melts (now glasses) found in xenoliths have different origins involving infiltration of melt/fluid and dissolution of primary silicates including amphibole, followed by the destabilization of spinel. Spinel experienced thus a late corrosion within a preexisting—likely hydrous—silicate melt. The secondary spinels that crystallized at the periphery of primary spinels are depleted in Al_2O_3 (Table 2), with subsequent Al-enrichment of the silicate melt.

Sample MG54. We can observe a weak increase of Al with decreasing Mg (Fig. 8). This can be interpreted as reflecting the accommodation of the spinel-derived Al_2O_3 molecules to the melt network according to the proposed reaction 1:

$$Al_2O_{3sp} + 3O^{2-}_{melt} \rightarrow 2(O_3Al)^{3-}_{melt} \quad (1)$$

The accommodation process proceeds necessarily through the breaking of several bonds of the silicate melt network. In reaction 1, three ≡Si-O-Si≡ covalent bonds are broken (the bond breaking is noted here as the consumption of three bridging O atoms, O^{2-}_{melt}) and both spinel-derived Al^{3+} ions are found as network-modifiers of the melt network. Two network-modifying units [noted $(O_3Al)^{3-}$, where Al^{3+} neutralizes three non-bridging O atoms] are consequently formed.

Sample MG102. Unlike in sample MG54, Al and Mg are here positively correlated and we also note an important increase of the K concentration with decreasing Mg, the lowest K concentration, at Mg ~ 2.1 at%, being four times lower in sample MG102 than in sample MG54 (Fig. 8). This can be interpreted as follows: the first Al_2O_3 molecules released from the dissolution of the MG102 spinels were essentially accommodated to the melt network after reaction 1. With the on-going dissolution of spinel, more and more Al_2O_{3sp} molecules were produced, which were accommodated to the melt network after the proposed reaction 2:

$$Al_2O_{3sp} + 2[K^+ + OH^-]_{aq} + 4O^{2-}_{melt} \rightarrow 2(AlO_4/K)^{4-}_{melt} + H_2O \quad (2)$$

The preceding reaction depicts how K^+ cations were extracted from a KOH phase, (noted $[K^+ + OH^-]_{aq}$), to stabilize Al^{3+} in the tetrahedral site, noted $(AlO_4/K)^{4-}_{melt}$. The presence of KOH-like complexes was suggested by Mysen and Acton (1999) in hydrated melts in the K_2O-Al_2O_3-SiO_2-H_2O system. The proposed present reaction 2 is just the right-to-left direction of reaction 3 found in Mysen and Acton (1999). The latter study supports the existence of a free aqueous fluid phase in addition to the melt in alkali aluminosilicate aqueous fluids. KOH complexes are unattached to the melt network and are probably part of the free aqueous phase. Dissolved H_2O in silicate melts is generally found as (nano-) phases disseminated throughout the melt network (e.g., Balcone-Boissard et al. 2009). However, given that water is mostly accommodated as bonded hydroxyls in basaltic melts (e.g., Lesne et al. 2011), it is likely that the KOH-bearing aqueous phase was reduced to a brine in our pre-erupted melts. Upon eruption, potassium ions were more and more easily extracted from KOH as they were more and more dissociated with increasingly rehydrated brine. Note also that K^+ is the preferred stabilizing ion in the tetrahedral site (e.g., Bottinga and Weill 1972; Pichavant et al. 1992 and reference therein) and thus, its extraction from the aqueous fluid predominates over the extraction of other alkalis such as Na. The breaking of four O^{2-}_{melt} is also required.

The evolutions of K and Al in both melts are schematically represented in Figure 9. The pressure-induced injection of the melt in the xenolith led to the corrosion of spinels accompanied by the release (dotted line) and the accommodation (solid lines) of Al_2O_{3sp} molecules after reactions 1 (dotted-dashed lines) and 2 (dashed lines). Reaction 1 dominates in the first stages of the accommodation process (few K + aqueous fluid → melt transfer). Reaction 2 becomes then more and more efficient, which is recorded as increasing K contents in melt networks with dropping Mg values. As Mg drops, the proposed mechanism results in an increasing gap between Al_2O_{3sp} molecules produced and accommodated to the melt network. As spinel corrosion proceeds with dehydration, more and more Al_2O_{3sp} molecules together with H_2O molecules are produced, which results in: (1) more and more Al_2O_{3sp} molecules to be transferred into the aqueous fluid and later exsolved, but in the same time, (2) more and more $(AlO_4/K)^{4-}_{melt}$ formed through reaction 2. The peculiar point where the Al content is dropping together with the increase of the K content can be seen in MG54 (Fig. 8). It corresponds presumably to the beginning of the dehydration process.

However, as shown on Figure 10, the melt/aqueous fluid exchanges are more complicated than those depicted in reaction 2. The amount of K extracted from the aqueous phase is exactly compensated by an amount of Ca that was likely transferred in the aqueous phase from the melt network, where Ca is known acting as a network-modifier (Fig. 10a). In addition the rate of variation of the K amount transferred from the aqueous phase is ca. two times higher than that of the amount of spinel-derived Al accommodated

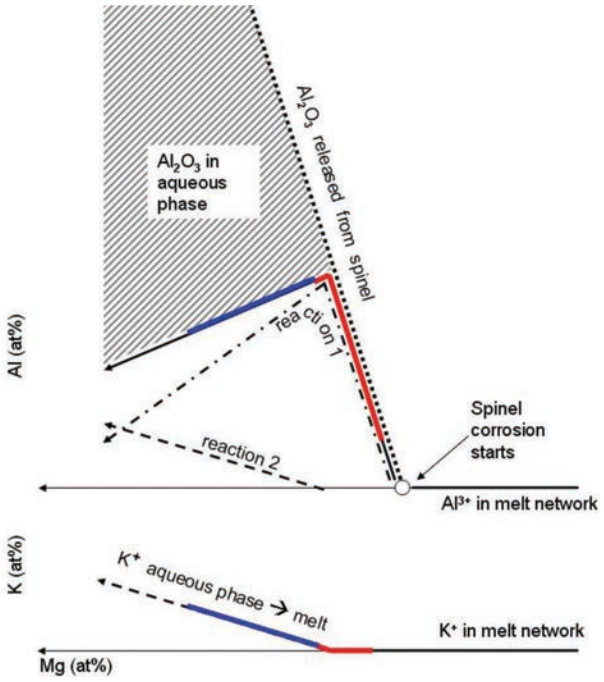

FIGURE 9. Schema of the evolution of K and Al vs. Mg for both MG54 and MG102 melts. Red lines = observed trends for MG54. Blue lines = observed trends for MG102. Note that, in accordance with Figure 8 for MG102, the blue line for K must be shifted down and that for Al must be shifted up (as less K and more Al relative to MG54 were present prior to reaction 2). See text for explanation. (Color online.)

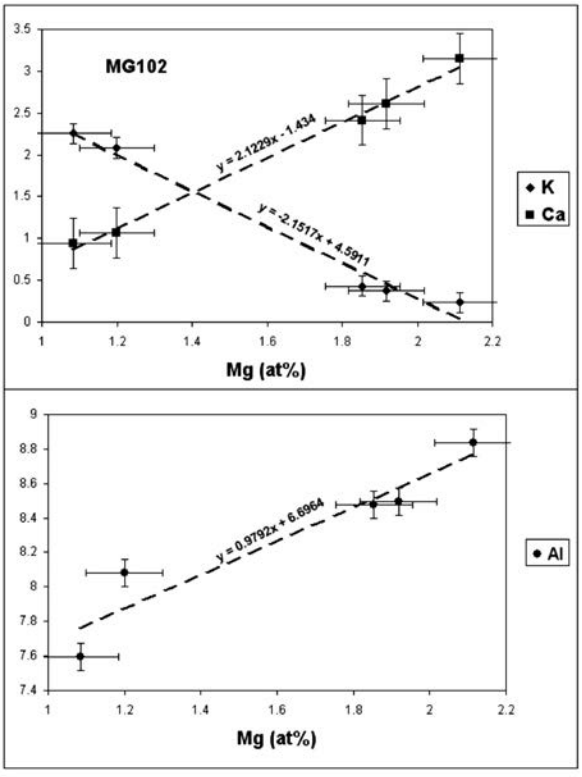

FIGURE 10. K, Ca, and Al variations (expressed in at%) vs. Mg in glasses from MG102.

in the melt network (Fig. 10b). Given that only a fraction of this Al is found in tetrahedral position with K as the stabilizer (Fig. 9), more K than necessary is extracted from the aqueous phase, which is in contradiction with reaction 2 (that depicts the common case where one K is required per AlO_4 to be stabilized). The following dehydration reaction 3 may resume these observations:

$$Al_2O_{3sp} + 4[K^+ + OH^-]_{aq} + 4(O_2Ca)^{2-}_{melt} + 2(OH)^-_{melt} \rightarrow 2(AlO_4/K)^{4-}_{melt} + 2(OK)^-_{melt} + 4CaO + 3H_2O \quad (3)$$

where $(O_2Ca)^{2-}_{melt}$ represents a network-modifying unit consisting of a Ca^{2+} ion neutralizing two non-bridging O atoms. Most CaO molecules produced were likely exsolved with H_2O upon eruption. Finally, two non-bridging O atoms formerly neutralized by two protons [forming a pair of bonded hydroxyls, $2(OH)^-_{melt}$] become now neutralized by two K^+ extracted from the aqueous phase. The major difference between reactions 2 and 3 is that no energy-consuming breaking of covalent bonds is required for reaction 3 in which sole network-modifying units are involved as reactants to result in a more polymerized melt.

Fe^{2+} oxidation

Glasses from the reaction pockets of sample MG54 were highly oxidized (HM ±1, hematite-magnetite buffer) compared to the original melt (FMQ ±1, fayalite-magnetite-quartz buffer) (Fialin et al. 2011). Similarly, glasses from sample MG102 also have high $Fe^{3+}/\Sigma Fe$, up to 0.99 in some pockets. The question of the origin of the oxidation process is discussed hereafter.

Superficial oxidation of the melt. In both samples, iron oxides were observed as fillings of cracks. We interpreted these cracks as having resulted from the release of mechanical stresses that occurred during the rapid cooling of the pocket melt (Fialin et al. 2011 for sample MG54). The width of the cracks is generally very small, which prevent accurate analysis with conventional microprobe or SEM. One of the largest (1.5–2 μm width) crack in MG54 was investigated in the present study with the EDS attached to the FE-SEM. The crack is not chemically homogeneous, composed of two phases at least. The microanalysis of these phases gave compositions that suggest hematite for the brightest part and a Mg-rich iron oxide (e.g., magnesioferrite, $MgFe^{3+}_2O_4$) for the other part (Fig. 11; Table 3). We can reasonably speculate that these hematite and magnesioferrite phases resulted from a very late oxidation mechanism that occurred at the same time as cracks were formed in the cooling glass. The mechanism of oxidation of a volcanic glass exposed to atmospheric oxygen has been described by, e.g., Cooper et al. (1996), Cook and Cooper (2000), and Minitti et al. (2002). Within this mechanism, glass oxidation is likely to proceed by surface-to-bulk diffusion of holes corresponding to the change of Fe^{2+} into Fe^{3+}, instead of diffusion of oxygen species (e.g., O_2). The hole diffusion is balanced by the migration to the free surface of network-modifying cations (Mg^{2+}, Ca^{2+}, Fe^{2+}, …) that form surfacial coatings of oxide species. The coprecipitation of MgO and Fe_2O_3 molecules would have so formed magnesioferrite

TABLE 3. Energy-dispersive analysis of both oxide phases depicted in Figure 11

	Hematite	±	Magnesioferrite	±
		wt%		
SiO_2	1.31	0.45	2.42	0.47
Al_2O_3	1.41	0.39	1.44	0.39
MgO	1.09	0.38	15.4	0.78
Cr_2O_3	1.77	0.41	1.43	0.42
Fe_2O_3	95.04	1.08	79.44	1.04
Total	100.61		100.03	
		at%		
Si	0.68		1.16	
Al	0.86		0.81	
Mg	0.84		10.96	
Cr	0.73		0.54	
Fe	37.17		28.51	
O	60.33		58.06	

Note: The error is estimated at 2σ; at% = atom percent. Standards used are the same as those used for the WDS analyses.

at the freshly formed air-crack interface. However, it must be pointed out that this mechanism only affects near surface layers (few micrometers) and, thus, does not involve bulk oxidation.

Has spinel corrosion induced the bulk melt oxidation? Melt oxidation is generally discussed by considering water as an oxidizing agent, although this remains highly debated (e.g., Crabtree and Lange 2012, and references therein; Cottrell and Kelley 2011, and references therein). The question is whether the Fe^{2+} oxidation can occur via the general reaction 4:

$$2FeO + H_2O \rightarrow Fe_2O_3 + H_2 \quad (4)$$

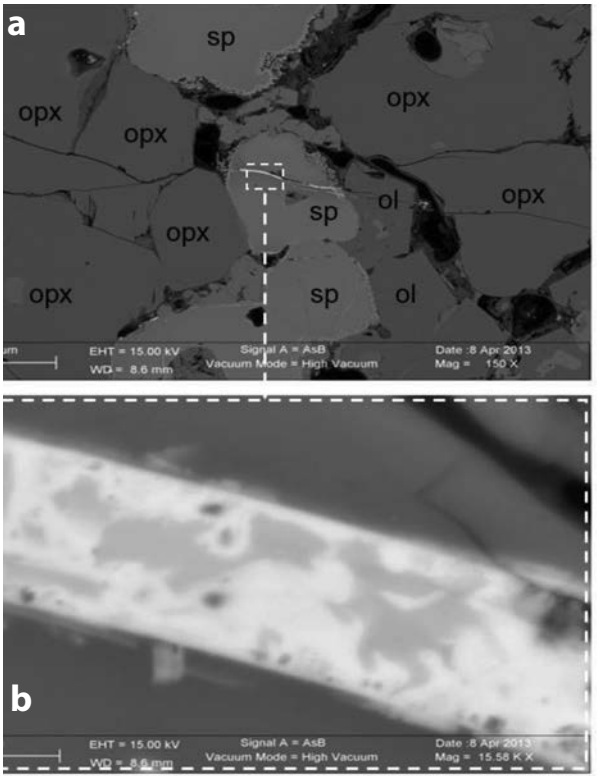

FIGURE 11. BSE images of a crack within sp in sample MG54 (**a**) filled with hematite in white and magnesioferrite in gray (**b**).

The production of H_2 via the reduction of H_2O is a key phenomenon that controls Fe^{2+} oxidation upon reducing conditions. The redox reaction 4 particularly applies via supercritical water/ultramafic rocks interactions in subduction zones with low-oxygen fugacities under standard temperature and pressure conditions, the so-called serpentinization process (e.g., Andreani et al. 2013 and references therein). Molecular hydrogen emissions are also detected as a surface degassing species from alkali magmas (e.g., Moussallam et al. 2012; and references therein). At higher P and T conditions in the mantle, H_2 may be a significant hydrous species dissolved in silicate liquids (Hirschmann et al. 2012). This means that some quantities of Fe^{3+} could be produced under high pressure as water is accommodated in silicate melt. Our present pocket melts exhibit f_{O_2} values for their pristine compositions falling within the range for subcontinental lithospheric mantle (FMQ ±1). These oxidized conditions prevent the degassing of sufficient H_2 to oxidize the melt FeO at the elevated levels measured. An alternative dehydrogenation process must be thus envisioned to explain the high-oxidation states of both melts.

In this respect, a relationship between the accommodation of Al_2O_{3sp} molecules (reactions 1 to 3) with the Fe^{2+} oxidation could be tentatively established. The major disadvantage of reaction 1 is to consume bridging O atoms to accommodate the spinel derived Al^{3+} to the melt network. Involving non-bridging O atoms would be less energy consuming as stated above for reactions 2 and 3. The concomitant accommodation of Al^{3+} and Fe^{3+} as network-modifiers can be written as the following dehydrogenation reaction 5:

$$Al_2O_{3sp} + 2(O_2Fe^{2+})^{2-}_{melt} + 2(OH)^{-}_{melt} \rightarrow 2(AlFe^{3+}O_4)^{2-}_{melt} + O^{2-}_{melt} + H_2 \quad (5)$$

Reaction 5 hypothesizes a Fe^{2+} oxidation mechanism involving the incorporation into a melt network of alumina produced by spinel dissolution. One network modifier Fe^{2+} complexes with one hydroxyl pair to result in the formation of two Al^{3+}- and Fe^{3+}-bearing anionic species as well as one hydrogen molecule. Within the ionic formalism used herein to describe the melt network, $(AlFe^{3+}O_4)^{2-}$ represents two non-bridging O atoms neutralized by one $(AlFe^{3+}O_2)^{2+}$ cationic complex (Fig. 12). Reaction 5 results in a more polymerized melt (production of one bridging oxygen). Replacing reaction 1 by reaction 5 in Figure 9 would indeed illustrate the observed increase followed by the drop of the $Fe^{3+}/\Sigma Fe$ ratios as Al_2O_{3sp} molecules were produced.

IMPLICATIONS

Percolating melts through a xenolith induce or contribute to the dissolution of host minerals. Then, the released mineral-forming constituents such as Al_2O_3 for spinel are accommodated to the melt network. In the first part of the present study we examined how spinel-derived Al_2O_3 molecules could have been accommodated to the melt network through the investigation of fresh glass sections found in reaction zones around variably corroded spinels. At an early stage of spinel dissolution (recorded by preserved melt compositions with $2 < Mg < 2.5$ at% in the MG54 sample), Al_2O_{3sp} molecules were presumably accommodated to the melt network through the formation of network modifying units (reaction 1). The investigation of reaction zones with highly corroded spinel (e.g.,

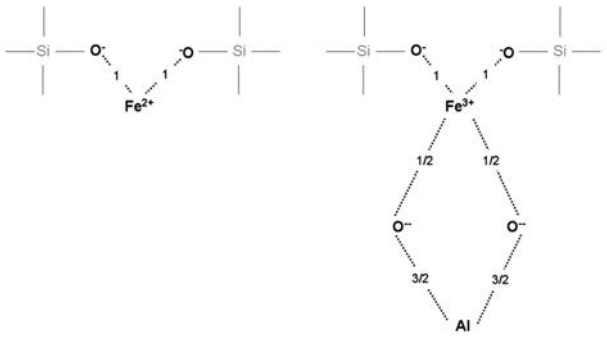

FIGURE 12. Schematics showing how a Fe^{2+} network modifier, represented here as neutralizing two non-bridging O atoms (**left**), can be oxidized through the formation of the bonded compound cation depicted in the dehydrogenation reaction 5 (**right**). Numbers refer to the number of electrons transferred from cations to O atoms.

zones 1 and 2 of the MG102 sample, 1 < Mg < 1.2 at%), showed that the spinel dissolution proceeded till the latest stage of eruption through the dehydration reaction 3. This reaction depicts how the $Al_2O_{3\ sp}$ molecules were ultimately accommodated to the melt as network-forming unit, noted $(AlO_4/K)^{4-}$. In this case, the tetrahedra stabilizing cations K^+ were extracted from the dehydrating melt.

Unlike the MG54 melt, the Al_2O_3 content of the MG102 melt dropped with dropping Mg, showing that more and more Al_2O_{3sp} molecules were exsolved as dehydration (and correlative spinel corrosion) proceeded. A Fe^{2+} oxidation mechanism induced by spinel corrosion is also proposed consisting in a dehydrogenation reaction accompanied with the formation of bonded anionic complexes associating spinel-derived Al^{3+} ions and Fe^{3+} ions formed by oxidation of Fe^{2+} network modifiers.

This study particularly shows how a melt percolating through a mineral assemblage can accommodate chemical elements released from minerals undergoing dissolution. This process could be related to important changes in the oxidation state of the melt.

ACKNOWLEDGMENTS

This study was financially supported by the CNRS (ISTeP) and CAMPARIS, Univ Paris 06. We thank D. Smith (Muséum National d'Histoire Naturelle) for the English revision of the paper. Critical reviews by C. Shaw and an anonymous reviewer greatly improved the paper. We thank R. Esposito for constructive comments and thorough editorial work.

REFERENCES CITED

Andreani, M., Muñoz, M., Marcaillou, C., and Delacour, A. (2013) μXANES study of iron redox state in serpentine during oceanic serpentinization. Lithos, 178, 70–83.

Balcone-Boissard, H., Baker, D.R., Villemant, B., and Boudon, G. (2009) F and Cl diffusion in phonolitic melts: Influence of the Na/K ratio. Chemical Geology, 263, 89–98.

Ban, M., Witt-Eickschen, G., Klein, M., and Seck, H.A. (2005) The origin of glasses in hydrous mantle xenoliths from the West Eifel, Germany: Incongruent break down of amphibole. Contributions to Mineralogy and Petrology, 148, 511–523.

Bottinga, Y., and Weill, D.F. (1972) The viscosity of magmatic silicate liquids: A model for calculation. American Journal of Science, 272, 438–475.

Carpenter, D.A., Edgar, A.D., and Thibault, Y. (2002) Origin of spongy textures in clinopyroxene and spinel from mantle xenoliths, Hessian depression, Germany. Mineralogy and Petrology, 74, 149–162.

Chazot, G., Menzies, M., and Harte, B. (1996) Silicate glasses in spinel lherzolites from Yemen: Origin and chemical composition. Chemical Geology, 134, 159–179.

Coltorti, M., and Grégoire, M. (2008) Metasomatism in oceanic and continental lithospheric mantle. Geological Society, London, Special Publication 293, 361 p.

Coltorti, M., Beccaluva, L., Bonadiman, C., Salvini, L., and Siena, F. (2000) Glasses in mantle xenoliths as geochemical indicators of metasomatic agents. Earth and Planetary Science Letters, 183, 303–320.

Cook, G.B., and Cooper, R.F. (2000) Iron concentration and the physical processes of dynamic oxidation in an alkaline earth aluminosilicate glass. American Mineralogist, 85, 397–406.

Cooper, R.F., Fanselow, J.B., and Poker, D.B. (1996) The mechanism of oxidation of a basaltic glass: Chemical diffusion of network-modifying cations. Geochimica et Cosmochimica Acta, 60, 3253–3265.

Cottrell, E., and Kelley, K.A. (2011) The oxidation state of Fe in MORB glasses and the oxygen fugacity of the upper mantle. Earth and Planetary Science Letters, 305, 270–282.

Crabtree, S.M., and Lange, R.A. (2012) An evaluation of the effect of degassing on the oxidation state of hydrous andesite and dacite magmas: A comparison of pre- and post-eruptive Fe^{2+} concentrations. Contributions to Mineralogy and Petrology, 163, 209–224.

Downes, H., and Dupuy, C. (1987) Textural, isotopic and REE variations in spinel peridotite xenoliths, Massif Central, France. Earth and Planetary Science Letters, 82, 121–135.

Downes, H., Reichow, M.K., Mason, P.R.D., Beard, A.D., and Thirlwall, M.F. (2003) Mantle domains in the lithosphere beneath the French Massif Central: trace element and isotopic evidence from mantle clinopyroxenes. Chemical Geology, 200, 71–87.

Draper, D.S., and Green, T.H. (1999) *P-T* phase relations of silicic, alkaline, aluminous liquids: new results and applications to mantle melting and metasomatism. Earth and Planetary Science Letters, 170, 255–268.

Féménias, O., Coussaert, N., Berger, J., Mercier, J.-C., and Demaiffe, D. (2004) Metasomatism and melting history of a Variscan lithospheric mantle domain: evidence from the Puy Beaunit xenoliths (French Massif Central). Contributions to Mineralogy and Petrology, 148, 13–28.

Fialin, M., Wagner, C., Métrich, N., Humler, E., Galoisy, L., and Bézos, A. (2001) $Fe^{3+}/\Sigma Fe$ vs. Fe-Lα peak energy for minerals and glasses: recent advances with the electron microprobe. American Mineralogist, 86, 456–465.

Fialin, M., Bézos, A., Wagner, C., Magnien, V., and Humler, E. (2004) Quantitative electron microprobe analysis of $Fe^{3+}/\Sigma Fe$: Basic concepts and experimental protocol for glasses. American Mineralogist, 89, 654–662.

Fialin, M., Wagner, C., and Pascal, M.-L. (2011) Iron speciation using electron microprobe techniques: Application to glassy melt pockets within a spinel lherzolite xenolith. Mineralogical Magazine, 75, 349–364.

Francis, D.M. (1976) The origin of amphibole in lherzolite xenoliths from Nunivak Island, Alaska. Journal of Petrology, 103, 277–286.

Frey, F.A., and Green, D.H. (1974) The mineralogy, geochemistry and origin of lherzolite inclusions in Victorian basanites. Geochimica et Cosmochimica Acta, 38, 1023–1059.

Granet, M., Wilson, M., and Achauer, U. (1995) Imaging a mantle plume beneath the French Massif Central. Earth and Planetary Science Letters, 136, 281–296.

Granet, M., Judenherc, S., and Souriau, A. (2000) Des images du système lithosphere-asthénosphère sous la France et leurs implications géodynamiques: l'apport de la tomographie télésismique et de l'anisotropie sismique. Bulletin de la Société Géologique de France, 171, 149–167.

Hirschmann, M.M., Withers, A.C., Ardia, P., and Foley, N.T. (2012) Solubility of molecular hydrogen in silicate melts and consequences for volatile evolution of terrestrial planets. Earth and Planetary Science Letters, 345–348, 38–48.

Hoernle, K., Zhang, Y.S., and Graham, D. (1995) Seismic and geochemical evidence for large-scale mantle upwelling beneath the eastern Atlantic and western and central Europe. Nature, 374, 34–38.

Ismail, M., Delpech, G., Cottin, J.-Y., Grégoire, M., Moine, B.N., and Bilal, A. (2008) Petrological and geochemical constraints on the composition of the lithospheric mantle beneath the Syrian rift, northern part of the Arabian plate. In M. Coltorti and M. Grégoire, Eds., Metasomatism in Oceanic and Continental Lithospheric Mantle. Geological Society, London, Special Publication, 293, 223–251.

Jardin, L. (1973) Les enclaves basiques et ultrabasiques dans les basaltes alcalins de la Chaîne du Devès (Haute Loire). Thèse de Doctorat de 3ème cycle, Université de Lyon, pp. 119.

Kushiro, I. (1975) On the nature of silicate melt and its significance in magma genesis: regularities in the shift of the liquidus boundaries involving olivine, pyroxene, and silica minerals. American Journal of Science, 275, 411–431.

Le Bas, M.J., Le Maitre, R.W., Streckeisen, A., and Zanettin, B.A. (1986) Chemical classification of volcanic rocks based on the total alkali–silica diagram. Journal of Petrology, 27, 745–750.

Lenoir, X., Garrido, C.J., Bodinier, J.-L., and Dautria, J.-M. (2000) Contrasting lithospheric mantle domains beneath the Massif Central (France) revealed by geochemistry of peridotite xenoliths. Earth and Planetary Science Letters, 181, 359–375.

Lesne, P., Scaillet, B., Pichavant, M., Iacono-Marziano, G., and Beny, J.-M. (2011) The H_2O solubility of alkali basaltic melts: An experimental study. Contributions to Mineralogy and Petrology, 162, 133–151.

Lo Cascio, M., Liang, Y., Shimizu, N., and Hess, P.C. (2008) An experimental study of the grain-scale processes of peridotite melting: implications for major and trace element distribution during equilibrium and disequilibrium melting. Contributions to Mineralogy and Petrology, 156, 87–102.

Maaloe, S., and Printzlau, I. (1979) Natural partial melting of spinel lherzolite. Journal of Petrology, 20, 727–741.

Maury, R., and Varet, J. (1980) Le volcanisme tertiaire et quaternaire. In A. Autran and J. Dercourt, Coord., Colloque C7. Géologie de la France, Mémoire du BRGM, 107, 138–159.

Mercier, J.C., and Nicolas, A. (1975) Textures and fabrics of upper-mantle peridotites as illustrated by xenoliths from basalts. Journal of Petrology, 16, 454–487.
Mergoil, J., and Boivin, P. (1993) Le Velay. Son volcanisme et les formations associées. Géologie de la France, 3, 3–96.
Minitti, M.E., Mustard, J.F., and Rutherford, J.R. (2002) Effects of glass content and oxidation on the spectra of SNC-like basalts: Application to Mars remote sensing. Journal of Geophysical Research, 107, 5030.
Moussallam, Y., Oppenheimer, C., Aiuppa, A., Giudice, G., Moussalam, M., and Kyle, P., (2012) Hydrogen emissions from Erebus volcano, Antarctica. Bulletin of Volcanology, 74-9, 2109–2120.
Mysen, B.O., and Acton, M. (1999) Water in H_2O-saturated magma–fluid systems; solubility behavior in K_2O-Al_2O_3-SiO_2-H_2O to 2.0 GPa and 1300 °C. Geochimica et Cosmochimica Acta, 63, 3799–3815.
Perinelli, C., Orlando, A., Conte, A.M., Armienti, P., Borrini, D., Faccini, F., and Misiti, V. (2008) Metasomatism induced by alkali magma in the upper mantle of northern Victoria Land (Antartica): An experimental approach. In M. Coltorti and M. Grégoire, Eds., Metasomatism in Oceanic and Continental Lithospheric Mantle. Geological Society, London, Special Publication, 293, 279–302.
Pichavant, M., Holtz, F., and, McMillan, P.F. (1992) Phase relations and compositional dependence of H_2O solubility in quartz-feldspar melts. Chemical Geology, 96, 303–319.
Shaw, C.S.J. (1999) Dissolution of orthopyroxene in basanitic magma between 0.1 and 2 GPa: Further implications for the origin of Si-rich alkaline glass inclusions in mantle xenoliths. Contributions to Mineralogy and Petrology, 135, 114–132.
——— (2009) Textural development of amphibole during breakdown reactions in a synthetic peridotite. Lithos, 110, 215–228.
Shaw, C.S.J., and Dingwell, D.B. (2008) Experimental peridotite-melt reaction at one atmosphere: a textural and chemical study. Contributions to Mineralogy and Petrology, 155, 199–214.
Shaw, C.S.J., and Klügel, A. (2002) The pressure and temperature conditions and timing of glass formation in mantle-derived xenoliths from Baarley, West Eifel, Germany: the case for amphibole breakdown, lava infiltration and mineral-melt reaction. Mineralogy and Petrology, 74, 169–187.
Shaw, C.S.J., Thibault, Y., Edgar, A.D., and Lloyd, F.E. (1998) Mechanisms of orthopyroxenes dissolution in silica-undersaturated melts at one atmosphere and implications for the origin of silica-rich glass in mantle xenoliths. Contributions to Mineralogy and Petrology, 132, 354–370.
Shaw, C.S.J., Heidelbach, F., and Dingwell, D.B. (2006) The origin of reaction textures in mantle peridotite xenoliths from Sal Island, Cape Verde: The case for "metasomatism" by the host lava. Contributions to Mineralogy and Petrology, 151, 681–697.
Stosch, H.G., and Seck, H.A. (1980) Geochemistry and mineralogy of two spinel peridotite suites from Dreiser Weiher, W. Germany. Geochimica et Cosmochimica Acta, 44, 457–470.
Su, B.-X., Zhang, H.-F., Asamoah Saki, P., Yang, Y.-H., Ying, J.-F., Tang, Y.J., Qin, K.-Z., Xiao, Y., Zhao, X.-M., Mao, Q., and Ma, Y.-G. (2011) The origin of spongy texture in minerals of mantle xenoliths from the Western Qinling, central China. Contributions to Mineralogy and Petrology, 615, 465–482.
Touron, S., Renac, C., O'Reilly, S.Y, Cottin, J.-Y., and Griffin, W.L. (2008) Characterization of the metasomatic agent in mantle xenoliths from Devès (France) using coupled in situ trace-element and O, Sr and Nd isotopic compositions. In M. Coltorti and M. Grégoire, Eds., Metasomatism in Oceanic and Continental Lithospheric Mantle. Geological Society, London, Special Publication, 293, 177–196.
Vanucci, R., Ottolini, L., Bottazi, P., Downes, H., and Dupuy, C. (1994) INAA, IDMS and SIMS comparative REE investigations of clinopyroxenes from mantle xenoliths with different textures. Chemical Geology, 118, 85–108.
Wagner, C., and Deloule, E. (2007) Behaviour of Li and its isotopes during metasomatism of French Massif Central lherzolites. Geochimica et Cosmochimica Acta, 71, 4279–4296.
Wang, Y., Han, B., Griffin, W.L., Zhang, L., and Shu, G. (2012) Post-entrainment mineral-magma interaction in mantle xenoliths from Inner Mongolia, western North China Craton. Journal of Earth Science, 23, 64–76.
Wilson, M., and Downes, H. (1991) Tertiary-Quaternary extension-related magmatism in western and central Europe. Journal of Petrology, 32, 811–849.
Xu, Y.G., Menziers, M.A., Bodinier, J.-L., Bedini, R.M., Vroon, P., and Mercier, J.-C. (1998) Melt percolation and reaction atop a plume: evidence from the poikiloblastic peridotite xenoliths from Borée (Massif Central, France). Contributions to Mineralogy and Petrology, 132, 65–84.
Yaxley, G.M., Kamenetsky, V., Green, D.H., and Falloon, T.J. (1997) Glasses in mantle xenoliths from Western Victoria, Australia, and their relevance to mantle processes. Earth and Planetary Science Letters, 148, 433–446.
Zangana, N.A., Downes, H., Thirlwall, M.F., and Hegner, E. (1997) Relationship between deformation, equilibration temperature, REE and radiogenic isotopes in mantle xenoliths (Ray Pic, Massif Central, France): An example of plume-lithosphere interaction? Contributions to Mineralogy and Petrology, 127, 187–203.

Manuscript received May 7, 2014
Manuscript accepted December 30, 2014
Manuscript handled by Rosario Esposito

Appendix

Appendix A: Petrographic description

Sample MG102 (Fig. 1) has a coarse-grained protogranular/porphyroclastic microstructure (according to the terminology of Mercier and Nicolas 1975). It contains large orthopyroxene (up to 5.3 mm) and olivine (up to 3.3 mm) with curvilinear crystal boundaries. Thin exsolution lamellae of clinopyroxene are sometimes observed in the larger orthopyroxene, whereas undulose extinction or kink band are rarely observed in olivine. Neoblasts of olivine are similar to those of sample MG54. Clinopyroxene and spinel are smaller (usually ~2 mm); clinopyroxene may exhibit a spongy texture depending of its location in the thin section, and interstitial brown Cr-spinel have a vermicular shape. Spinels from zones 1 and 2 show large reaction zones compared to spinels from the other zones 3 and 4 (Fig. 1).

Sample MG54 (Fig. 2) has a microstructure intermediate between protogranular and porphyroclastic-tabular (Mercier and Nicolas 1975). It is medium-grained with larger (2–3 mm)—sometimes kink-banded—olivine and orthopyroxene than clinopyroxene and brown Cr-spinel (1–2 mm). Smaller polygonal and annealed neoblasts of olivine may exhibit typical 120° triple junctions. The sample shows discontinuous alignments of Cr-spinels surrounded by reaction zones, in which pargasite occurs as a few small (100–150 μm) and often rounded inclusions in pyroxene (Fig. 2d).

Appendix B: Chemical composition of the primary and secondary silicate minerals

In both samples, primary olivine, orthopyroxene, and clinopyroxene (diopside) are in chemical equilibrium with high mg* [mg* = 100 × molar $Mg/(Mg + Fe^{2+})$] of 90–91, although clinopyroxene may be slightly more magnesian (mg* up to 93). They are homogeneous and show no compositional gradients whatever their location in the xenolith, next to the basanite contact or in the interior of the xenolith, and close—or not—to reaction pockets. In sample MG54, amphibole is a pargasite less magnesian (mg* = 86–87) and richer in TiO_2 and Cr_2O_3 (~1.6 and 1.3 wt%, respectively) than clinopyroxene. Primary diopside contains 0.2–0.6 wt% of TiO_2, <1 wt% Cr_2O_3, and ~6 wt% of Al_2O_3 in sample MG54 compared to 4–6 wt% in sample MG102, and more variable (2.5–6 wt%) content in the sieved clinopyroxene from the latter.

In the reaction pockets orthopyroxene has never been found as secondary crystals. Secondary olivine from both samples has mg* similar to primary olivine and higher CaO content (0.1–0.2 wt%). Secondary clinopyroxene is a diopside close to the limit with augite, it has similar mg* than primary clinopyroxene. In sample MG54, secondary clinopyroxene is richer in TiO_2 and Cr_2O_3 (1–2 wt% and up to 2.1 wt%, respectively) and has higher and more variable Al_2O_3 (6–8 wt%), whereas Na_2O is lower (0.6–0.8 wt%) compared to primary diopside (1.2–1.8 wt%). In sample MG102, secondary clinopyroxene shows higher Cr_2O_3 (1.1–1.8 wt%) and slightly lower Na_2O (~1 wt%), whereas TiO_2 and variable Al_2O_3 contents are similar to those of primary diopside.